Radio-based Sensing and Indoor Mapping with Millimeter-Wave 5G NR Signals

Carlos Baquero Barneto, Taneli Riihonen, Matias Turunen, Mike Koivisto, Jukka Talvitie, and Mikko Valkama
Tampere University, Electrical Engineering, Tampere, Finland
carlos.baquerobarneto@tuni.fi

***Abstract*—The emerging 5G New Radio (NR) networks are expected to enable huge improvements, e.g., in terms of capacity, number of connected devices, peak data rates and latency, compared to existing networks. At the same time, a new trend referred to as the RF convergence is aiming to jointly integrate communications and sensing functionalities into the same systems and hardware platforms. In this paper, we investigate the sensing prospects of 5G NR systems, with particular emphasis on the user equipment side and their potential for joint communications and environment mapping. To this end, a radio-based sensing approach utilizing the 5G NR uplink transmit signal and an efficient receiver processing and mapping scheme are proposed. An indoor scenario is then studied and evaluated through real-world RF measurements at 28 GHz mm-wave band, showing that impressive mapping performance can be achieved by the proposed system. The measurement data is available at a permanent open repository.**

***Index Terms*—5G New Radio (NR), joint communications and sensing, RF convergence, indoor mapping, mm-waves.**

I. Introduction

The emerging 5G New Radio (NR) networks are evolving to support and facilitate a wide range of new services, while providing huge improvements in terms of, e.g, peak data rates, network capacity, number of connected devices, and radio access latency, compared to earlier Long-Term Evolution (LTE) based systems [1]. At the same time, a new trend referred to as the RF convergence is becoming an increasingly important research area that aims to develop joint communication and sensing (JCAS) systems that can perform both functionalities while sharing the same transmit waveforms and hardware platforms [2], [3]. JCAS solutions based on 5G networks represent a very timely research opportunity [4]–[8].

One key capability of 5G NR systems concerns the user equipment (UE) positioning accuracy, which should be in the order of one meter or even below according to the latest specifications [9]. This is technically achieved by the exploitation of wide bandwidths at mm-wave frequencies, combined with directional antenna arrays that together enable highly accurate time-based and angle-based measurements and, hence, high-accuracy positioning [5]. The 5G NR Release 15 [1] includes new operating bands within the range of 24.25 GHz–52.6 GHz, supporting channel bandwidths up to 400 MHz, while allows for antenna arrays with 256 and 64 elements at network and UE sides, respectively. Additionally, it is noted that 5G NR supports orthogonal frequency-division multiple access (OFDMA) in both downlink and uplink.

This work was partially supported by the Academy of Finland (grants #310991, #315858, #328214, #319994), Nokia Bell Labs, and the Doctoral School of Tampere University. The work was also supported by the Finnish Funding Agency for Innovation under the "RF Convergence" project.
Measurement data available at https://doi.org/10.5281/zenodo.3754175 [15].

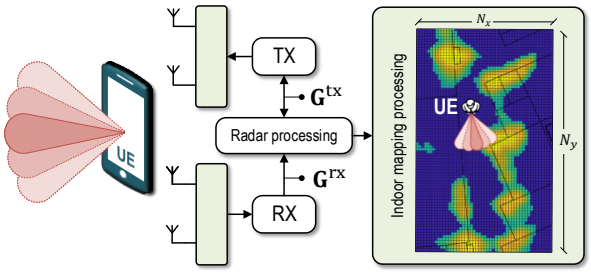

Fig. 1. Considered joint communication and sensing/radar scenario in mm-wave 5G NR network, for user terminal based mapping applications.

In general, in expected 5G *outdoor* deployments at mm-waves with densely distributed access nodes (ANs), a single UE is most likely within the coverage range of multiple ANs – an issue that is further contributing to reaching positioning accuracies below one meter [9]. However, the mm-wave propagation characteristics make the positioning much more challenging in *indoor* environments. To overcome these difficulties, a few recent studies have raised the idea of using simultaneous localization and mapping (SLAM) schemes in order to achieve such 5G positioning requirements also in indoor scenarios [10]–[13]. To this end, in [10], [11], a personal mobile radar concept operating at mm-waves and consisting of massive arrays for environmental mapping is proposed. Similarly, [12] proposes a SLAM-based architecture to perform localization through obstacle detection and dimensioning for indoor environments using mm-wave frequencies. In [13], a message passing-based estimator, which jointly estimates the position and orientation of the UE while sensing the environment's reflectors, is presented. However, due to the challenges of performing RF measurements at mm-wave bands, very few works have supported their mm-wave SLAM-based approaches with empirical results to assess and demonstrate the performance with real hardware [10], [11].

In this work, we present a user-centric 5G mm-wave indoor mapping system and method. In the proposed system, the user device senses the surrounding environment by steering its beam pattern towards different directions and collecting the target reflections utilizing the NR uplink transmit signal as illustrated

978-1-7281-6455-7/20/$31.00 ©2020 IEEE

conceptually in Fig. 1. The associated radar/sensing techniques are described in Section II, together with the proposed grid-based mapping processing methods. Indoor office measurement environment and utilized mm-wave hardware are described in Section III, while the actual RF measurement results at the 28 GHz band [15] and their analysis are provided in Section IV. The obtained results experimentally verify that the proposed system is able to accurately map the environment.

II. System Model and Mapping Processing

A. OFDM-based Radar Processing

The indoor mapping functionality in the NR UE builds on the known uplink transmit orthogonal frequency-division multiplexing (OFDM) waveform. In particular, the considered mobile device, equipped with phased arrays in both transmit (TX) and receive (RX) chains, senses its environment by steering its beam pattern towards different directions and collecting the target reflections in order to reconstruct the surrounding scenario as illustrated in Fig. 1.

Similar to classical OFDM-radar literature [4], [5], [14], we consider frequency-domain radar processing which directly works on the uplink NR frequency-domain resource grid, of size $S \times R$, that contains the frequency-domain samples of S consecutive active subcarriers and R OFDM symbols. At the TX side, the baseband uplink waveform is generated by block-wise IFFT operating in the uplink NR frequency-domain resource grid, together with cyclic prefix addition.

Considering specific steering direction θ, the uplink transmit waveform interacts with one or multiple targets of the indoor environment, producing reflections that are simultaneously collected by the RX phased array. The received signal containing the target reflections is demodulated and processed through FFT to obtain the corresponding receive grid. The distance and the relative speed of a target k correspond to the propagation delay τ_k and the Doppler shift $f_{\mathrm{D},k}$, respectively. With K point targets, the receive grid sample on pth subcarrier and qth OFDM symbol can be expressed as

$$G^{\mathrm{rx}}_{p,q} = \sum_{k=1}^{K} b_k G^{\mathrm{tx}}_{p,q} e^{2\pi j(qT_{\mathrm{s}} f_{\mathrm{D},k} - p\tau_k \Delta f)} + G^{\mathrm{noise}}_{p,q}, \qquad (1)$$

where $G^{\mathrm{tx}}_{p,q}$ and $G^{\mathrm{noise}}_{p,q}$ represent the TX signal's and the receiver thermal noise's grid samples on pth subcarrier and qth OFDM symbol, respectively. The subcarrier spacing is denoted by Δf while T_{s} denotes the total OFDM symbol duration, including the cyclic prefix duration. The parameter b_k models the effective attenuation of the kth target reflection.

In this work, similar to, e.g., [4], [5], [14], we adopt subcarrier-domain processing with a channel estimation-like scheme. The parameters τ_k and $f_{\mathrm{D},k}$ are calculated by element-wise division of the receive and transmit grids as

$$G_{p,q} = \frac{G^{\mathrm{rx}}_{p,q}}{G^{\mathrm{tx}}_{p,q}} = \sum_{k=1}^{K} b_k e^{2\pi j(qT_{\mathrm{s}} f_{\mathrm{D},k} - p\tau_k \Delta f)} + \tilde{G}^{\mathrm{noise}}_{p,q}. \qquad (2)$$

The delay/range profile is then calculated in terms of discretized time delay τ, based on the periodogram of the matrix (2) containing the delay and Doppler information of the sensed environment, and expressed as [14]

$$\Phi(\tau) = \frac{1}{R}\left|\sum_{q=0}^{R-1}\left(\sum_{p=0}^{S-1} G_{p,q} W_{p,q} e^{j2\pi p\,\tau \Delta f}\right)\right|^2, \qquad (3)$$

where the inner IFFTs of size S correspond to delay profiles of each OFDM symbol. In addition, the signal-to-noise ratio is improved by coherent integration of R delay profiles. The estimated delay/range profiles are discretized according to $\tau_s = \frac{s}{S\Delta f}$ where $s \in [0, S-1]$. Windowing can be also applied by including appropriate weights $W_{p,q}$ which control the sidelobe level of Φ. For simplicity, this work ignores the Doppler processing and consequently, the ability of distinguish between static and moving targets. However, this can be easily implemented by an extension of (3) as shown in [4], [14].

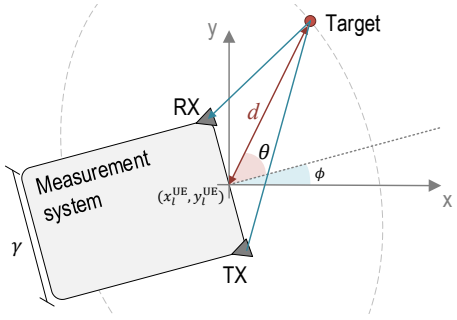

Fig. 2. System model geometry. The measurement system located at $\left(x_l^{\mathrm{UE}}, y_l^{\mathrm{UE}}\right)$ with orientation ϕ senses the environment at a steering angle θ detecting a target with distance d.

B. System Geometry

In typical monostatic radars, where TX and RX antennas are co-located, the target distance can be easily estimated by considering that the received signal is delayed by the same time when travels to the target and back. However, in this work, we used a quasi-monostatic configuration, where the TX and RX antennas are not located in the same position as illustrated in Fig. 2. We assume an ellipse-based model to correct the targets' time delay τ depending on the steering direction θ that can be written as

$$d(\tau, \theta) = \frac{\tau c_0}{2}\sqrt{\frac{(\tau c_0)^2 - \gamma^2}{(\tau c_0)^2 - \gamma^2 \cos^2\theta}}, \qquad (4)$$

where c_0 is the speed of light and γ corresponds to the separation between TX and RX antennas. It can be observed that this distance correction factor is especially sensitive for targets with distances with the same order of magnitude as the parameter γ. Notice that the estimated distance for very large propagation delays in comparison with the antenna separation $\tau c_0 \gg \gamma$, can be approached by the general expression for the monostatic case: $d \approx \frac{\tau c_0}{2}$.

C. Grid-based Mapping Processing

In this work, we consider a grid-based mapping approach to create a planar map of the surrounding environment by using

the UE radar/sensing functionality at different L locations while the antenna beams are steered to different I azimuth angles. Each of the calculated delay/range profiles contain S discretized samples, giving a total of $A = L \times I \times S$ measured points.

Considering a UE location $\left(x_l^{\text{UE}}, y_l^{\text{UE}}\right)$ with $l \in [0, L-1]$, the targets' Cartesian coordinates are calculated including the distance correction factor described in (4) as

$$\begin{aligned} x_a &= x_l^{\text{UE}} + d\left(\tau_s, \theta_i\right) \cos\left(\theta_i + \phi\right), \\ y_a &= y_l^{\text{UE}} + d\left(\tau_s, \theta_i\right) \sin\left(\theta_i + \phi\right), \end{aligned} \tag{5}$$

where $a = \{s + iS + lSI, \forall s, \forall i, \forall l\}$ and the parameter $\theta_i = \theta_{\text{min}} + \Delta\theta\,(i-1)$ where $i \in [0, I-1]$ refers to the set of steering directions with minimum steering angle θ_{min} and beam step of $\Delta\theta$. The parameter ϕ denotes the UE orientation angle as illustrated in Fig. 2. Similarly, the delay/range profiles for different steering angles and UE locations are defined as

$$z_a = \Phi_{l,i}\left(\tau_s\right). \tag{6}$$

In the proposed grid-based map, the environment is discretized creating a grid of $N_{\text{total}} = N_{\text{x}} \times N_{\text{y}}$ cells as illustrated in Fig. 1. Each of the cells contains the average of the range profiles over all the targets whose coordinates are within that cell. Therefore, the map grid sample on the αth vertical cell and the βth horizontal cell, can be described as

$$M_{\alpha,\beta} = \frac{\sum_{a \in \mathcal{M}_{\alpha,\beta}} z_a}{\mathcal{C}\left\{\mathcal{M}_{\alpha,\beta}\right\}}, \tag{7}$$

where $\mathcal{M}_{\alpha,\beta} = \left\{a \mid \left(x_a \in \boldsymbol{\chi}_\beta\right) \cap \left(y_a \in \boldsymbol{\psi}_\alpha\right), \forall a\right\}$. The parameters $\boldsymbol{\chi}_\beta = [\chi_{\beta,\text{min}}, \chi_{\beta,\text{max}}]$ with $\beta \in \{0, \ldots, N_{\text{x}} - 1\}$ and $\boldsymbol{\psi}_\alpha = [\psi_{\alpha,\text{min}}, \psi_{\alpha,\text{max}}]$ with $\alpha \in \{0, \ldots, N_{\text{y}} - 1\}$ refer to the horizontal and vertical ranges of the cell $M_{\alpha,\beta}$, respectively. The operator $\mathcal{C}\{\cdot\}$ denotes the cardinality of the set and consequently the total number of targets within a specific cell. Then, a convolution or kernel matrix is applied to extract certain features from the original average grid map (7). In general, the filtered grid map samples can be expressed as

$$\tilde{M}_{\alpha,\beta} = \sum_{u=-U}^{U} \sum_{v=-V}^{V} \Omega_{u,v} M_{\alpha-u,\beta-v}, \tag{8}$$

where Ω refers to the kernel matrix with $-U \leq u \leq U$ and $-V \leq v \leq V$. In this work, we assume a square Gaussian kernel matrix with $U = V$ and standard deviation σ for both vertical and horizontal domains described as

$$\Omega_{u,v} = \frac{1}{2\pi\sigma^2} \exp\left[-\frac{u^2 + v^2}{2\sigma^2}\right]. \tag{9}$$

Finally, individual filtered grid map samples are subject to a threshold test, expressed as

$$\tilde{M}_{\alpha,\beta} \underset{H_1}{\overset{H_0}{\lessgtr}} T_{\text{th}}, \tag{10}$$

where T_{th} denotes the detection threshold, H_0 refers to the null hypothesis, while H_1 refers to the alternative hypothesis. Specifically, if $\tilde{M}_{\alpha,\beta} > T_{\text{th}}$, the detector declares that the target is present in that specific cell, while if $\tilde{M}_{\alpha,\beta} < T_{\text{th}}$, it declares that no target is detected.

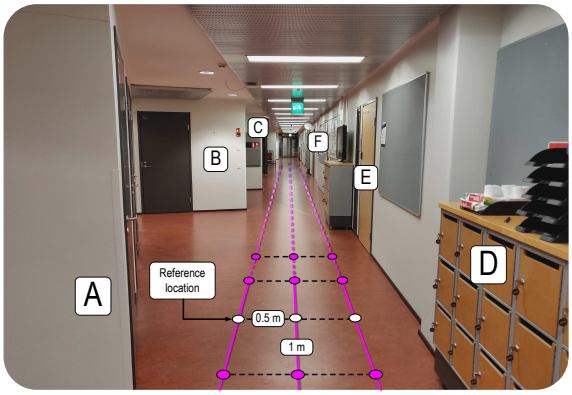

(a)

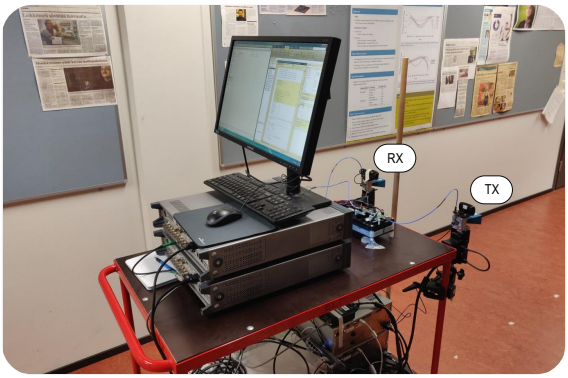

(b)

Fig. 3. (a) The measurement scenario including the main test locations and most important radar targets. (b) The main equipment used in the mapping measurements.

III. Measurement Campaign

A. Scenario Description

A measurement campaign was conducted at an indoor office environment in Hervanta Campus of Tampere University as shown in Fig. 3(a). The considered heterogeneous environment consist of a corridor of 2 m width and 60 m long with different office rooms in both sides. The corridor was measured along three parallel reference lines of 30 m with a distance step of one meter, providing a total of 93 test locations. In addition, these positions were tested in both directions along the corridor, providing a total of six sets of measurements. In Fig. 3(a), the considered test locations as well as the most significant targets from the radar perspective are shown. We can highlight three walls that are perpendicular to the system trajectory—*A*, *B* and *C*—located at the left side of the figure. Moreover, at the right side, three metal lockers—*D*, *E* and *F*—are expected to be the main reflective targets.

B. Measurement Setup

The equipment used for the indoor mapping measurements, with a carrier frequency of 28 GHz are shown in Fig. 3(b). All the measurement equipment are mounted on a trolley to enable moving smoothly through the indoor scenario. The measurements were conducted with a vector signal transceiver

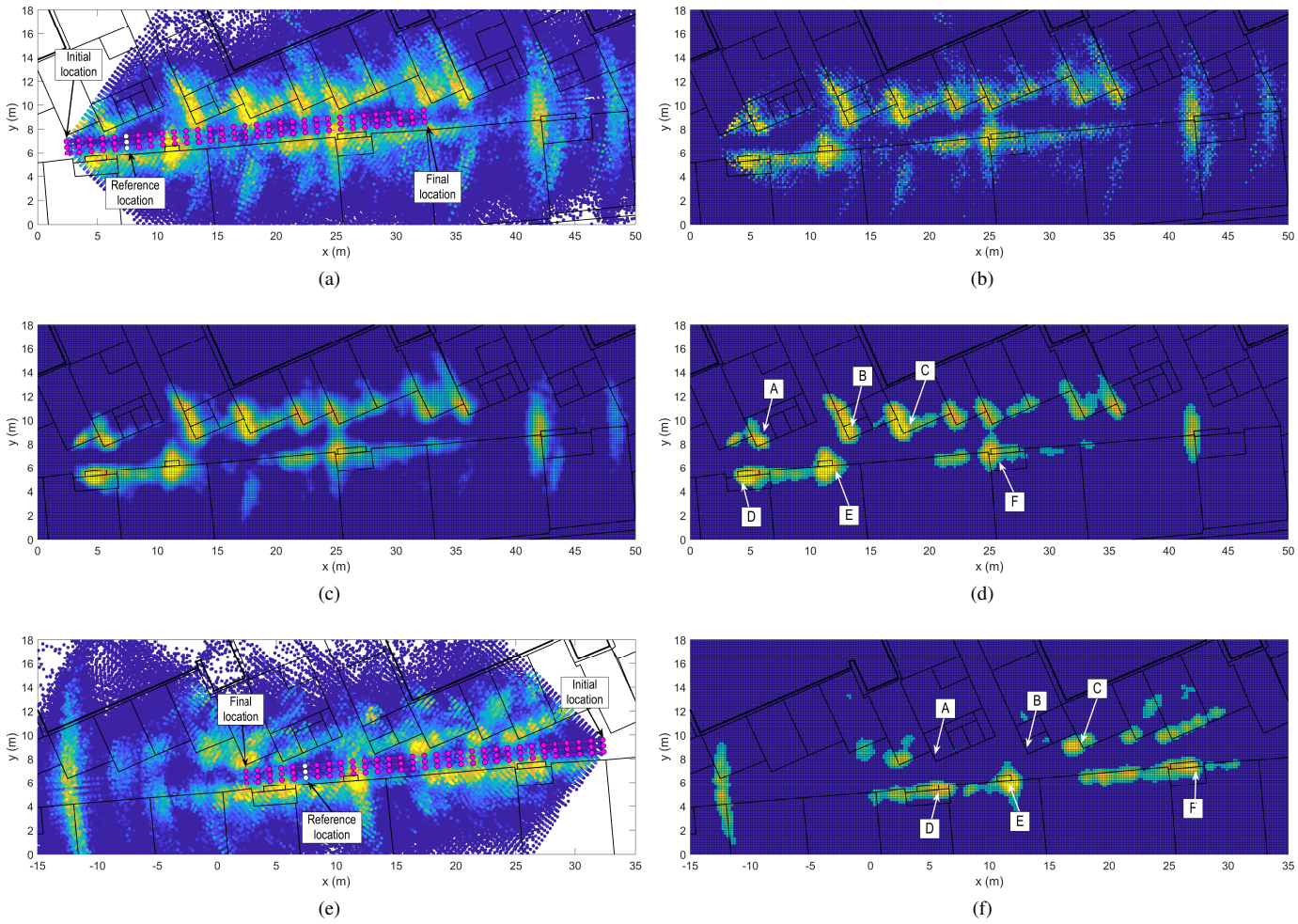

Fig. 4. Indoor mapping measurements at mm-wave using a 5G measurement system. Subfigures (a), (b), (c) and (d) correspond to mapping measurements from left part of the corridor to right as shown in (a). Subfigure (a) illustrates the sensing measurements from the highlighted locations. The corresponding grid-based maps (b), (c) and (d) illustrate the average sensing measurements, the map after applying a kernel matrix and the map after threshold test decision, respectively. Similarly, (e) and (f) show the sensing and final mapping results for the opposite measurement direction.

(PXIe-5840) which implements the RF transmitter and receiver functionalities at intermediate frequency of 3.5 GHz, as well as controls the rest of the devices. In addition, two signal generators are used as local oscillators (N5183B–MXG), together with external mixers to up/down-convert the IF signal to/from the desired mm-wave carrier frequency.

The UE's phased array operation is emulated by using directive horn antennas (PE9851A-20) for both TX and RX sides. They are mounted on mechanical steering systems which enable to steer and direct the horns in the whole azimuth plane. Both horns provide a nominal gain of 20 dBi with a 3 dB beam width of 17°. The antennas are placed at one meter above the floor level, with a separation of 60 cm in order to avoid larger mutual coupling between TX and RX chains. In the TX side, two external power amplifiers (PA) are used that together with the antenna system facilitate an EIRP of +20 dBm.

In the measurements, OFDM-based NR uplink waveform with the widest available mm-wave channel bandwidth of 400 MHz and subcarrier spacing of 120 kHz is utilized [1]. In particular, we consider an uplink NR frequency-domain resource grid with $S = 3168$ active subcarriers and $R = 28$ OFDM symbols corresponding to an observation window of around 0.25 ms. According to [5], the considered transmit waveform provides a basic range resolution of about 0.4 m and a maximum range of around 100 m. The subcarrier-domain radar processing is implemented as described in Section II-A.

IV. Mapping Results

In this section, the obtained indoor mapping measurement results—available at a permanent open repository [15]—are presented and analyzed to assess and demonstrate the performance of the proposed joint communication and radar system. We first measure the corridor in one direction—from left to right according to Fig. 4(a)—through three parallel lines at $L = 93$ different locations. In each of the locations, the measurement trolley is placed also parallel to the measurement lines with an orientation of $\phi = 5°$ with respect to the x-axis, while radar measurements are performed for $I = 51$ steering angles

between -50° to 50° with a step of 2°. We apply the radar and mapping processing techniques described in Section II-C obtaining the results shown in Fig. 4. In this figure, the building layout map and the main target locations are included for reference.

Figure 4(a) presents the obtained sensing measurements of all considered locations shown with markers. In addition, a reference location is highlighted in white for comparison with Fig. 3(a). Range profiles are obtained and distance correction is applied according to (3) and (4) using a basic rectangular window. It can be seen that the proposed system is able to accurately sense the fairly complex environment making mapping reconstruction that clearly represents the main scenario layout. Most of the detected targets correspond to the corridor walls. However, there are also some reflections that seem to come from inside the rooms. We noticed that some of these targets are due to double reflections in the environment that can be easily removed with the presented averaging, filtering and threshold steps discussed shortly. Another aspect important to emphasize is the limited angular resolution of the system due to the antenna beam width. Especially, when the targets are placed far from the system, they produce elongated shapes that can decrease the mapping performance. Limiting the range of the measurements can reduce this effect.

We then implement the proposed grid-based mapping processing to create a 2D map of the corridor with $N_{\mathrm{x}} = 225$ and $N_{\mathrm{y}} = 90$ using square cells with size of $0.2 \times 0.2\ m^2$, which is consistent with the range resolution of about 0.4 m. First, we reconstruct a map that contains the average intensity of the different range profiles in each cell as illustrated in Fig. 4(b). With this step, we focus the targets' intensity into more specific cells while the negative effects of the double reflections and the angular resolution are potentially decreased.

Next, a Gaussian kernel matrix is applied to the average grid map in order to smooth the map and reduce possible map noise. The kernel design parameters are set as $U = V = 5$ and $\sigma = 1$. Alternative kernel matrices can be also applied to extract different map features. Fig. 4(c) illustrates the filtered map showing smoother and more homogeneous targets.

Finally, the grid map is subject to a threshold test to emphasize the most important targets of the environment as illustrated in Fig. 4(d). This threshold can be adjusted depending on the sensed environment and the targets to be detected. It can be observed how the proposed system is able to impressively reconstruct the sensed environment. We specially highlight the main corridor walls' (*A*, *B* and *C*) and the metallic lockers' (*D*, *E* and *F*) locations for better comprehension of the final result.

In addition, we also analyze how the mapping system performance is subject to the UE orientation by showing sensing and final mapping results done along the corridor's opposite direction as illustrated in Fig. 4(e) and Fig. 4(f), respectively. In this case, we assume the same setup and processing parameters as above. These new results show how new targets are detected, while some other targets such as the walls *A*, *B* and *C* vanish, when the trolley is moved along a different direction. Consequently, several different measurements can be combined in order to obtain a more rich and accurate representation of the environment.

V. Conclusions

This paper investigated the 5G NR sensing potential with specific emphasis on the UE side and user-centric joint communication and sensing methods for indoor mapping at mm-wave frequencies. In the considered system, the UE senses its surrounding environment by steering its beam pattern towards different directions and collects the target reflections utilizing an NR uplink transmit signal. This is then complemented with OFDM-based radar and grid-based mapping processing techniques that were described in the paper. The applicability of the proposed methods was demonstrated, in the context of indoor mapping, through actual RF measurements at the 28 GHz band. The obtained results indicate impressive mapping reconstruction in the considered indoor office scenario.

References

[1] "3GPP TS 38.104 v15.4.0, "NR; Base Station (BS) radio transmission and reception", Tech. Spec. Group Radio Access Network, Rel. 15," Dec. 2018.

[2] B. Paul, A. R. Chiriyath, and D. W. Bliss, "Survey of RF communications and sensing convergence research," *IEEE Access*, vol. 5, pp. 252–270, 2017.

[3] F. Liu, C. Masouros, A. Petropulu, H. Griffiths, and L. Hanzo, "Joint radar and communication design: Applications, state-of-the-art, and the road ahead," *CoRR*, 2019, available at: https://arxiv.org/abs/1906.00789.

[4] C. Baquero Barneto *et al.*, "Full-duplex OFDM radar with LTE and 5G NR waveforms: Challenges, solutions, and measurements," *IEEE Trans. Microw. Theory Tech.*, vol. 67, no. 10, pp. 4042–4054, Oct. 2019.

[5] C. Baquero Barneto, M. Turunen, S. D. Liyanaarachchi, L. Anttila, A. Brihuega, T. Riihonen, and M. Valkama, "High-accuracy radio sensing in 5G New Radio networks: Prospects and self-interference challenge," in *Proc. Asilomar Conf. Signals, Syst., Computers (ASILOMAR)*, Nov. 2019.

[6] M. L. Rahman, J. A. Zhang, X. Huang, Y. J. Guo, and R. W. Heath Jr, "Framework for a perceptive mobile network using joint communication and radar sensing," *IEEE Trans. Aerosp. Electron. Syst.*, 2019.

[7] C. Baquero Barneto *et al.*, "Multibeam design for joint communication and sensing in 5G New Radio networks," in *Proc. 2020 IEEE Int. Conf. Commun. (ICC'20)*, Dublin, Ireland, Jun. 2020.

[8] S. D. Liyanaarachchi *et al.*, "Joint OFDM waveform design for communications and sensing convergence," in *Proc. 2020 IEEE Int. Conf. Commun. (ICC'20)*, Dublin, Ireland, Jun. 2020.

[9] M. Koivisto *et al.*, "High-efficiency device positioning and location-aware communications in dense 5G networks," *IEEE Commun. Mag.*, vol. 55, no. 8, pp. 188–195, Aug. 2017.

[10] F. Guidi, A. Guerra, and D. Dardari, "Personal mobile radars with millimeter-wave massive arrays for indoor mapping," *IEEE Trans. Mobile Comput.*, vol. 15, no. 6, pp. 1471–1484, Jun. 2016.

[11] F. Guidi *et al.*, "Indoor environment-adaptive mapping with beamsteering massive arrays," *IEEE Trans. Veh. Technol.*, vol. 67, no. 10, pp. 10 139–10 143, Oct. 2018.

[12] A. Yassin, Y. Nasser, A. Y. Al-Dubai, and M. Awad, "MOSAIC: Simultaneous localization and environment mapping using mmWave without a-priori knowledge," *IEEE Access*, vol. 6, pp. 68 932–68 947, 2018.

[13] R. Mendrzik *et al.*, "Joint localization and mapping through millimeter wave mimo in 5G systems," in *Proc. IEEE Global Communications Conference (GLOBECOM)*, Dec. 2018, pp. 1–6.

[14] M. Braun, "OFDM radar algorithms in mobile communication networks," Ph.D. dissertation, Karlsruhe Institute of Technology, 2014.

[15] C. Baquero Barneto *et al.*, "Dataset for radio-based sensing and indoor mapping with millimeter-wave 5G NR signals," 2020. [Online]. Available: https://zenodo.org/record/3754175